Paper 063

CODE TO CODE COMPARISON OF AIRCRAFT-MODE TILT-ROTOR AERODYNAMICS

L. Vigevano[1], M. Biava[1], P. Beaumier[2], J. Decours[2], W. Khier[3], T. Kneisch[4]

[1] Dipartimento di Ingegneria Aerospaziale - Politecnico di Milano, Italy [2] ONERA, Meudon, France
[3] DLR, Braunschweig, Germany [4] Eurocopter Deutschland, Ottobrunn, Germany

Abstract

A global comparison of several blind-test numerical predictions of the aerodynamic field around the Erica model in aircraft mode, carried out by some Partners of the *NICETRIP* consortium, is presented. The calculations are carried out with different codes, different turbulence models, different wind tunnel setups and different grids, with the objective of supporting the future experimental test campaign in the DNW-LLF and ONERA S1Ma wind tunnels. It is found that the level of unsteadiness introduced by the rotor wake on the aerodynamic loads on the fuselage, wing and nacelle may be relevant. The influence of the lower-mounted wind tunnel support is rather limited, while the rear-mounted support introduces some local unsteady effects on the fuselage loads. The overall qualitative agreement of the pressure distributions among different calculations is acceptable, while the scatter of the quantitative average loads is somewhat important.

1 Introduction

To investigate the aerodynamic characteristics of the ERICA (Enhanced Rotorcraft Innovative Concept Achievement) concept, a highly sophisticated, motorized, 1/5 scale model of the Erica tilt-rotor design has been manufactured and assembled for an experimental test campaign that will take place in the DNW-LLF and ONERA S1Ma wind tunnels in the framework of the *NICETRIP* European project. As a support for the experiments, pre-test blind calculations in aircraft-mode configuration were carried out by some Partners of the *NICETRIP* consortium.

The computations differ by both numerical tools and grids used. Time-accurate unsteady simulations were performed by ONERA with the *elsA* code, DLR with the *FLOWer* code, Politecnico di Milano (PoliMi) with the *ROSITA* code, while unsteady simulations with an uniformly loaded Actuator Disk (AD) rotor model were completed by Eurocopter Deutschland (ECD) with the *FLOWer* code. ONERA and PoliMi used the same Chimera grid assembly, that reproduces the model mounted in the S1Ma tunnel with a rear sting, while DLR and ECD represents the model in the DNW-LLF tunnel with a belly support sting, using similar but different grid sets. All Chimera grid systems have been generated so as to allow the calculation of different geometrical configurations, as required for the conversion operating conditions of the tilt-rotor aircraft. The computed configuration refers to the aircraft-mode operation at $M = 0.18$ and $Re = 1.7 \times 10^6$, based on the model wing mean chord.

The paper presents a global comparison of the achieved results, which allow assessing the relative influence of the numerical methods, turbulence models and grids on the aerodynamic loads and flow field features. It is organized as follows: section 2 briefly summarizes the main characteristic of the employed CFD solvers; section 3 reports the numerical parameters of the simulations and the general characteristics of the grid systems used; the achieved numerical results are compared and discussed in section 4 and the conclusions of the comparison exercise are drawn in the last section.

2 Description of the flow solvers

The numerical simulations presented and discussed hereinafter are based on the time-accurate solution of the Unsteady Reynolds (Favre) Averaged Navier-Stokes (URANS) equations in three dimensions by means of three CFD block-structured, finite volume codes: *elsA* [1] by ONERA, *FLOWer* [2] by DLR and ECD, and *ROSITA* [3] by PoliMi. Several features of the numerical methods employed in the present study are similar among the solvers: cell-centered finite volume spatial discretization on multi-block structured grids, formulated as to account for moving and deforming meshes satisfying the geometry conservation law, central discretization of the viscous fluxes, time integration using the dual-time stepping method [4], moving Chimera technique to facilitate the grid generation process and represent the motion of the blades in the simulation, characteristic-type boundary conditions, parallelization making use of the MPI framework. There are however some noticeable differences in the presented simulations, regarding the spatial discretization of the convective fluxes, the integration approach in pseudo-time, the turbulence models, the details of the adopted Chimera algorithms.

2.1 Convective fluxes

In the present *FLOWer* simulations, the convective fluxes are discretized with second order central differences. Third order numerical dissipation is added to the convective fluxes to ensure numerical stability. These dissipative contributions are reduced to first order when a shock is detected. Smooth transition from the third to the first order is realized by linear combination of both terms. A similar approach is followed in *elsA* computations, which make use of the 2$^{\text{nd}}$ order Jameson scheme with a scalar artificial viscosity including Martinelli's correction.

The *ROSITA* solver makes use of the Roe's scheme [5]. Second order accuracy is obtained through the use of MUSCL extrapolation supplemented with a modified version of the Van Albada limiter introduced by Venkatakrishnan [6].

2.2 Pseudo-time integration

As noticed, all codes adopt the dual-time approach for unsteady calculations, with different ways of performing the pseudo-time integration.

In *FLOWer* calculations, the pseudo-time integration is carried out by an explicit Runge-Kutta scheme. Convergence is accelerated by local time stepping, implicit residual smoothing and the multigrid method.

In the present *elsA* simulations a backward Euler time integration is used, with a LU-SSOR scalar relaxation implicit phase.

The *ROSITA* code employs a 2$^{\text{nd}}$ order backward differentiation formula to approximate the time derivative and a fully unfactored implicit scheme in pseudo-time. The generalized conjugate gradient (GCG), in conjunction with a block incomplete lower-upper preconditioner, is used to solve the resulting linear system.

2.3 Turbulence models

FLOWer contains a large array of statistical turbulence models, ranging from algebraic and one-equation eddy viscosity models to seven-equation Reynolds stress model. In this work a slightly modified version of Wilcox's two-equation $k-\omega$ model is used [7]. Unlike the main flow equations, Roe's scheme is employed to compute the turbulent convective fluxes.

Among the several turbulence models available in *elsA*, the Kok $k-\omega$ model [8] with SST correction has been used for the present simulations.

The one-equation Spalart-Allmaras model [9] is used in the *ROSITA* simulations.

2.4 Chimera algorithms

The implementation of the Chimera approach in *FLOWer* follows the ideas of Benek [10]. Theoretically, an unlimited number (up to the code dimension limits) of hierarchies of relative motions can be specified in time, and applied to the different elements of the geometry. Each level of the hierarchy defines a separate reference frame in which motions can be specified independently of the inertial frame of reference, thus allowing any combination of translation and rotation motions to be realized by a series of simple co-ordinate transformations. The search for cells, required for

interpolation, is performed by an Alternating Digital Tree (ADT) search method. The hole cutting procedure does not imply any hierarchical mesh dependencies: to mark points being inside a solid body, a simple auxiliary grid which encloses the solid body must be provided by the user. All points of the grid inside the auxiliary grid are excluded from the flow calculation. This leaves uncontrolled the extent of the overlapping regions within the domain. Special corrections are applied to overlapping regions located close to solid walls [11].

PoliMi's approach has a similar generality about the relative motion of the solid bodies, but follows a different approach for hole cutting and tagging, which is derived from that originally proposed by Chesshire and Henshaw [12], with modifications to improve robustness and performance. The tagging procedure accounts for a hierarchical grid ordering and attempts to minimize the overlap regions. To speed up the search of donor points, both oct-tree and ADT data structures are considered.

Among the several methods and parameters available in *elsA* to adapt the mask and interpolation to the Chimera configuration, for the present simulations the ADT method (Alternating Digital Tree) is used with one cell interpolation outside the mask, made of Cartesian elements.

All codes employ non-conservative tri-linear interpolation to transfer information among the different grids. For integration of the aerodynamic forces on overlapping surface grids, a special treatment proposed by Chan and Buning [13] is used.

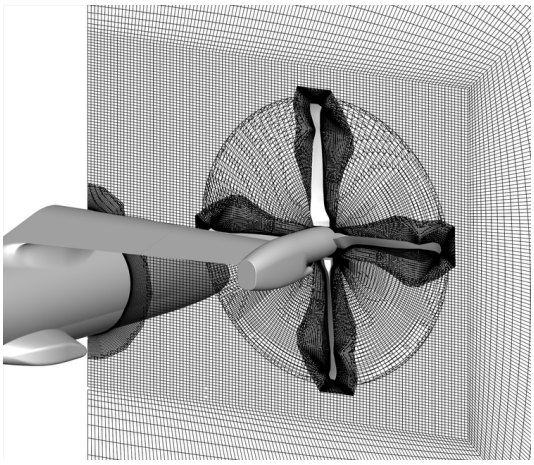

Figure 1: Characteristics of ONERA/PoliMi grids

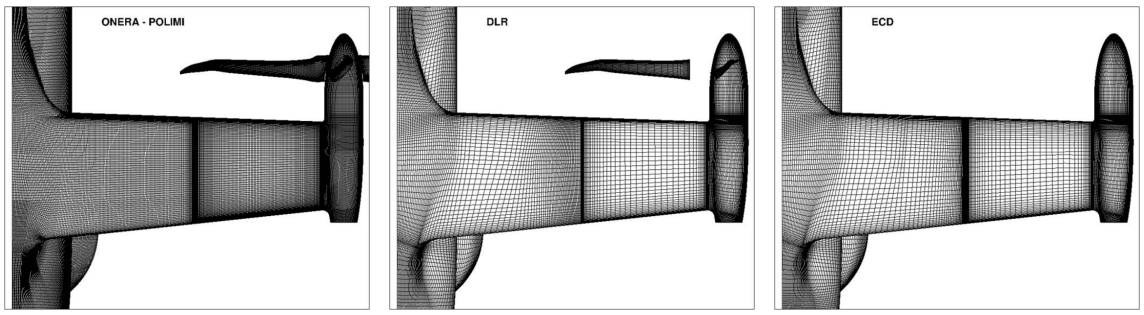

(a) ONERA and PoliMi grid (b) DLR grid (c) ECD grid

Figure 2: Surface grids on the wing

3 Grid characteristics and numerical details

ONERA and PoliMi cooperated in generating an overlapping grid assembly for the rear-support configuration to be tested in the $8\,m$ diameter circular test section of the S1Ma wind tunnel. The resulting grids have the following general characteristics:

- relatively high density of the surface discretization
- small extension of the fuselage and wing grids, away from the solid surface (see fig. 1)
- large extension of the nacelle grid, which encompasses almost entirely the rotor diameter, for wake capturing purposes
- Cartesian background grid

This grid system allows for a 2 mm gap between fixed and tiltable wing and fully represents the blade root, leaving a small gap between blade and spinner.

DLR and ECD generated overlapping grid sets for the lower support configuration to be tested in the $9.5 \times 9.5\,m^2$ test section of the DNW-LLF wind tunnel. The grid set generated by DLR accounts for a 1 mm gap between fixed and tiltable wing and does not represents the blade root. ECD calculations have been carried out with a slightly modified version of DLR grid, which accounts for a local refinement in the inter-wing gap region and replace the rotor blade grids with an annular grid, in order to use the Actuator Disk (AD) model of the rotor itself. DLR and ECD grids present a slightly less refined surface discretization than ONERA/PoliMI grids, as illustrated by fig. 2.

The dimensions of the grid used are reported in table 1.

More details on the surface discretization of the different components will be given in the next section when discussing the computed results.

All time-accurate calculations have been carried out with a time step corresponding to a 1 deg of rotor revolution, being the rotating speed 2450 rpm. They differ for the number of sub-iterations performed in pseudo-time, which have been selected 20 for ONERA, 50 for PoliMi and 50-100 for DLR, the latter figure referring to the final time period of the computation.

	ONERA/PoliMi	DLR	ECD
Fuselage and fixed wing	5.8	11.7	8.63
Tiltable wing	2.0	0.72	0.73
Nacelle	3.8	3.6	4.06
Rotor blade (×4)	4.0	2.2	–
Actuator disc	–	–	0.4
Sting	0.15	0.35	1.2
Wind tunnel	6.8	0.47	2.71
Total	22.55	19.04	17.73

Table 1: Volume grid dimensions, given in number of nodes $\times 10^6$

4 Discussion of results

All calculations refer to the aircraft-mode configuration of the 1/5 ERICA model installed in the wind tunnel. The considered tunnel operating conditions differ slightly among the Partners as reported in table 2, resulting in a slightly higher free-stream velocity considered by PoliMi with respect to the other Partners.

The computed results will be analyzed considering the aircraft components separately.

	V_∞ [m/s]	T_∞ [K]	P_∞ [Pa]	M_∞	support
ONERA	62.82	318	88802	0.176	rear-mounted
PoliMI	64.13	316	86965	0.18	rear-mounted
DLR	62.0	308	101325	0.176	belly-mounted
ECD	62.82	316	86965	0.176	belly-mounted

Table 2: Wind tunnel operating conditions

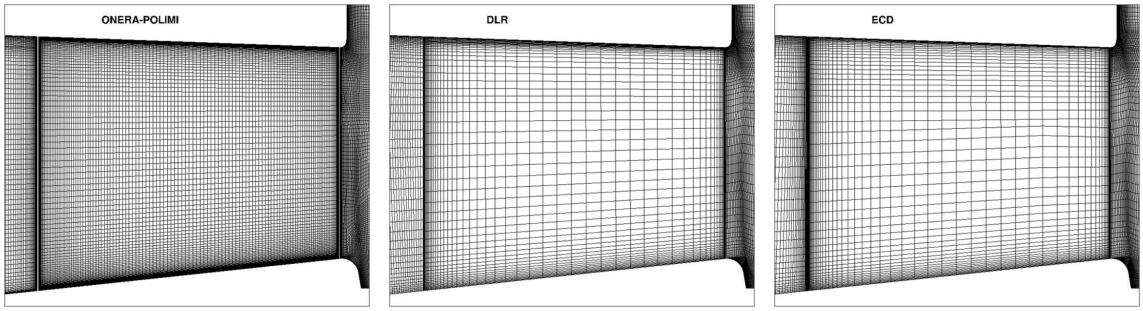

(a) ONERA and PoliMi grid (b) DLR grid (c) ECD grid

Figure 3: Detail of the surface grids on the tiltable wing

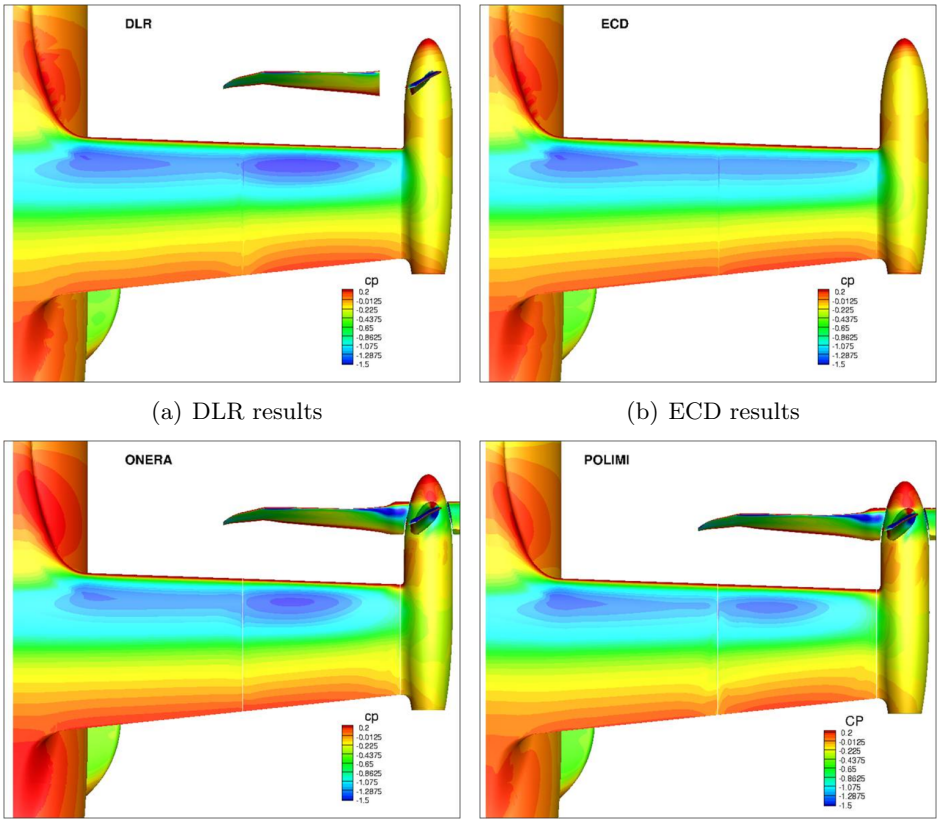

(a) DLR results (b) ECD results

(c) ONERA results (d) PoliMi results

Figure 4: Pressure field on the upper wing side

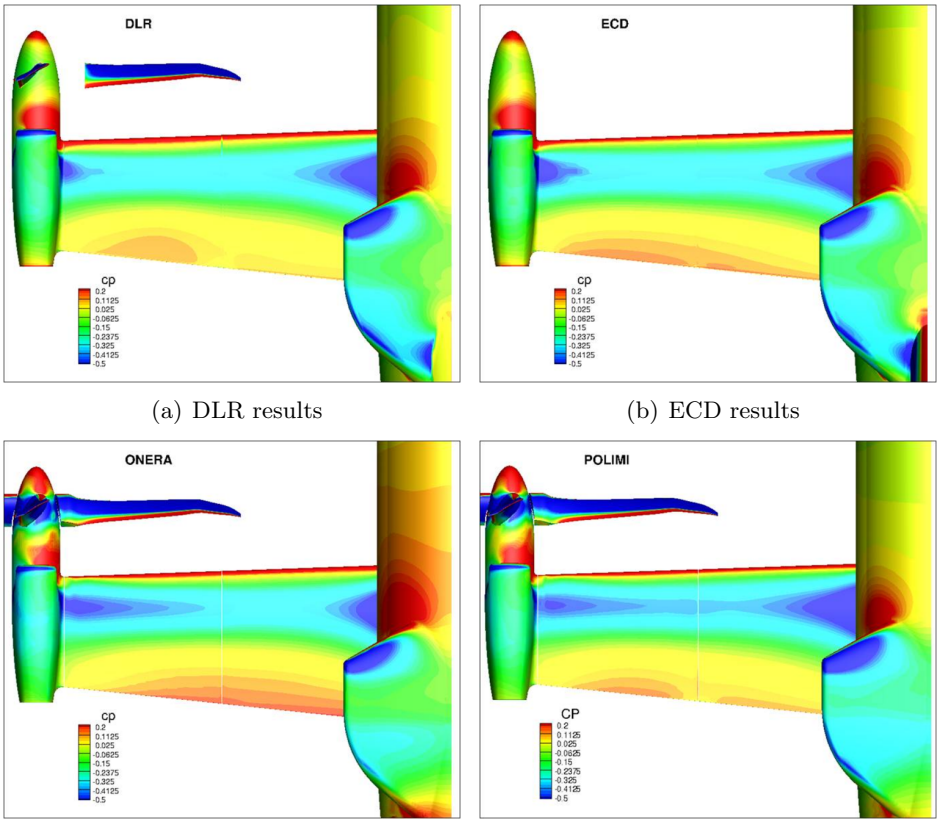

(a) DLR results (b) ECD results

(c) ONERA results (d) PoliMi results

Figure 5: Pressure field on the lower wing side

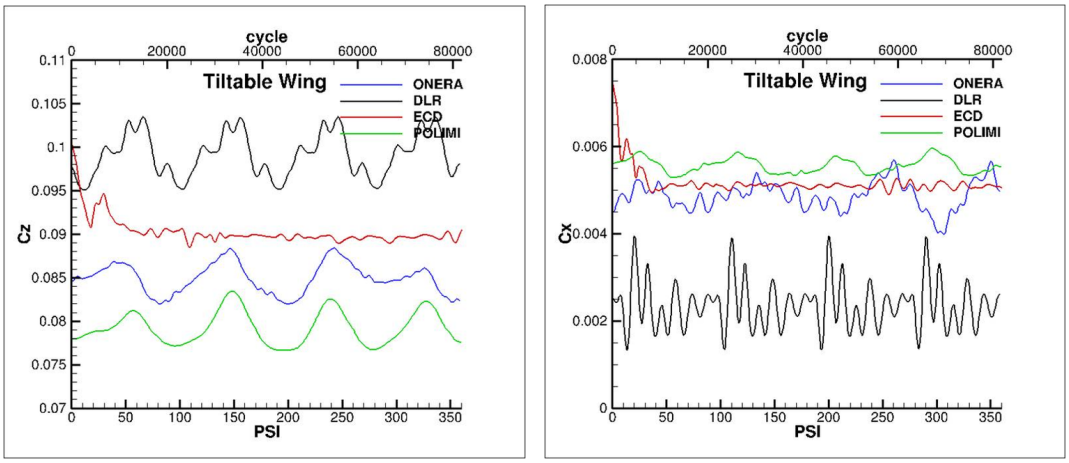

(a) Cz (b) Cx

Figure 6: Global loads on the tiltable wing

4.1 Wing

A detail of the surface grids on the tiltable wing is given in fig. 3, where the different grid density between ONERA/PoliMi and DLR/ECD calculations can be observed. The instantaneous pressure distribution on the wing upper surface at $\psi = 0\,\text{deg}$, which corresponds to the lower vertical position of the reference blade, is shown in fig. 4. The influence of the rotor induced flow on the pressure of the tiltable wing upper side is clearly observed in the time-accurate ONERA, PoliMi and DLR results, while it is much less pronounced in the ECD AD calculations. A stronger influence of the flow within the gap between fixed and tiltable wing is shown by DLR and PoliMi results. In the latter calculations it is clearly observed a turbulent jet escaping from the gap already at 50% of the chord. On the wing lower side (fig. 5) the calculations are qualitatively very similar, with again a stronger influence of the gap flow in PoliMi and DLR results, and some differences in the outer wing region, close to the nacelle, between ONERA/PoliMi and DLR/ECD results, the latter due to the difference in surface discretization density and possibly to the explicit representation of the blade root in the ONERA/PoliMi simulations.

The global loads on the tiltable wing are reported in fig. 6, during one rotor revolution. A noticeable 4/rev lift distribution (fig. 6(a)) is observed in all calculations, with DLR results also showing a higher frequency content. The spreading of the average lift values of the time-accurate computations is within ±10% to the steady ECD value. We recall here that ECD simulations are carried out with a time-accurate approach but with steady-state boundary conditions.

The computed average drag coefficient is very similar for the Partners, with the exception of DLR results, which predict a noticeably lower average value, together with higher unsteadiness.

4.2 Nacelle

The surface grids on the nacelle inner side are reported in fig. 7, where the representation of the blade root in the ONERA/PoliMi grid is evidenced, together with the higher density of the surface discretization. The corresponding pressure distributions are shown in fig. 8, where it can be observed that the local influence of the blade root is very strong, even if in the aft part of the nacelle the pressure level becomes very similar for all computations. The effect of the presence of the blade root reduces noticeably the lift contribution of the nacelle, see fig. 9(a). The average values of the drag coefficient for the nacelle present a relatively high scatter, with the larger value predicted by the steady AD calculations.

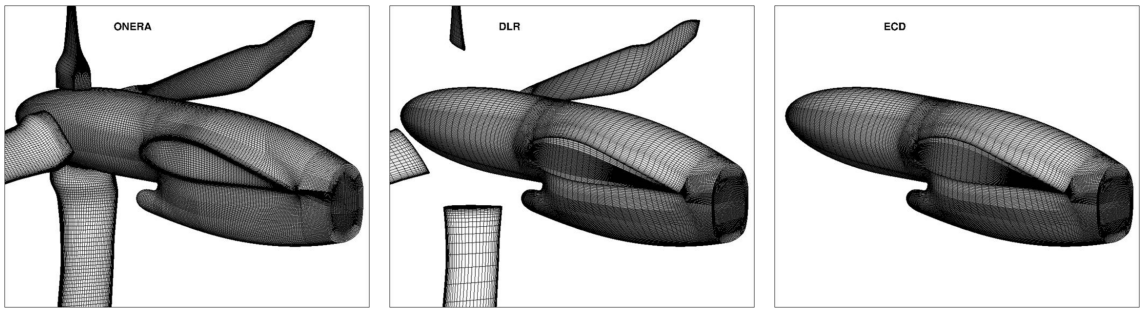

(a) ONERA and PoliMi grid (b) DLR grid (c) ECD grid

Figure 7: Surface grids on the nacelle inner side

4.3 Fuselage

The pressure distribution on the front part of the fuselage is quite similar for all computations, as shown in fig. 10, implying a small influence of the type of support. Please note that the support is not depicted in the DLR results although present in the simulation. Some differences may be observed in the higher pressure regions located below the wing root and in front of the sponson, especially in ONERA results, where the value of the

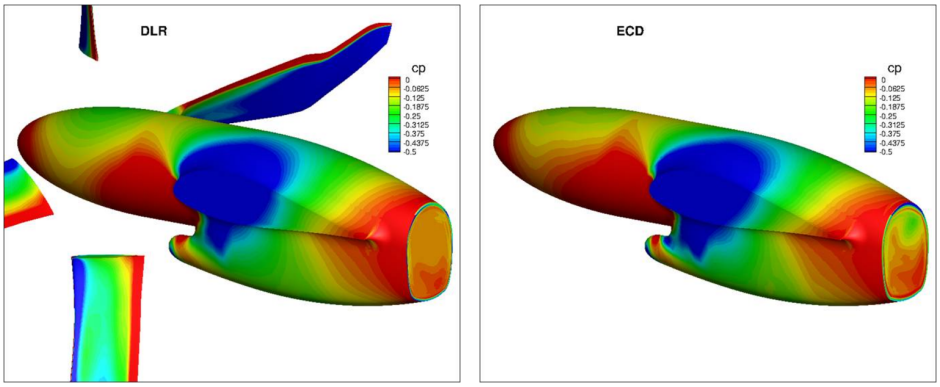

(a) DLR results (b) ECD results

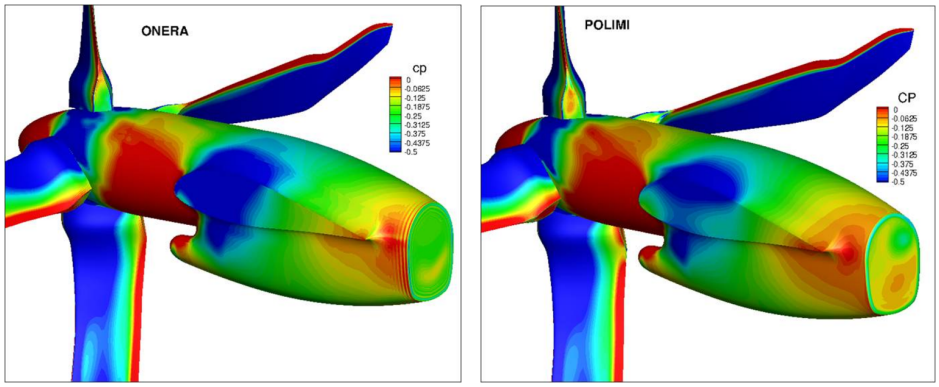

(c) ONERA results (d) PoliMi results

Figure 8: Pressure field on the nacelle inner side

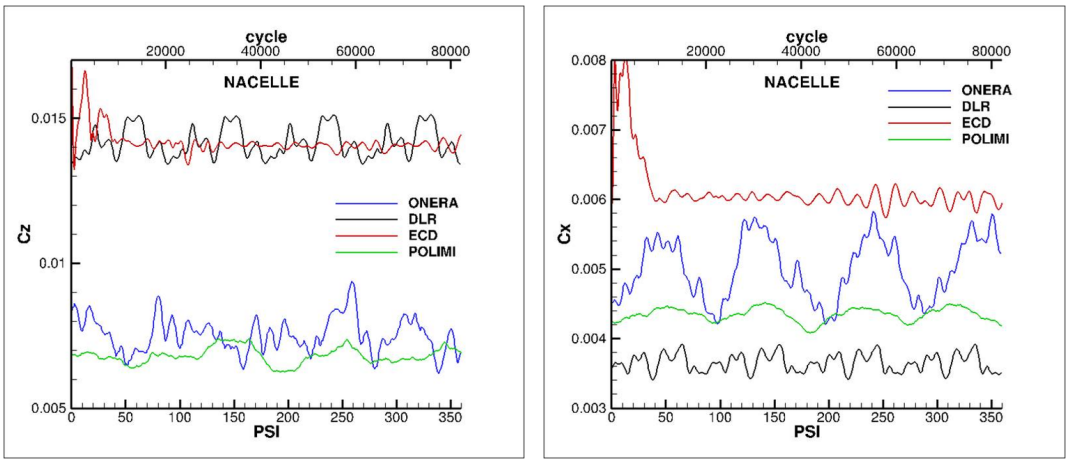

(a) Cz (b) Cx

Figure 9: Global loads on the nacelle

pressure coefficient is larger than in other calculations. The local influence of the lower-mounted support is very limited in the DLR and ECD calculations, while a slightly larger effects is produced by the rear-mounted support in the ONERA and PoliMi calculations (see fig. 11). Notwithstanding a rather good qualitative comparison of the pressure distributions, the quantitative lift coefficient in fig. 12(a) shows different behaviors. The rear-mounted support configuration introduces a higher degree of unsteadiness of the global fuselage loads.

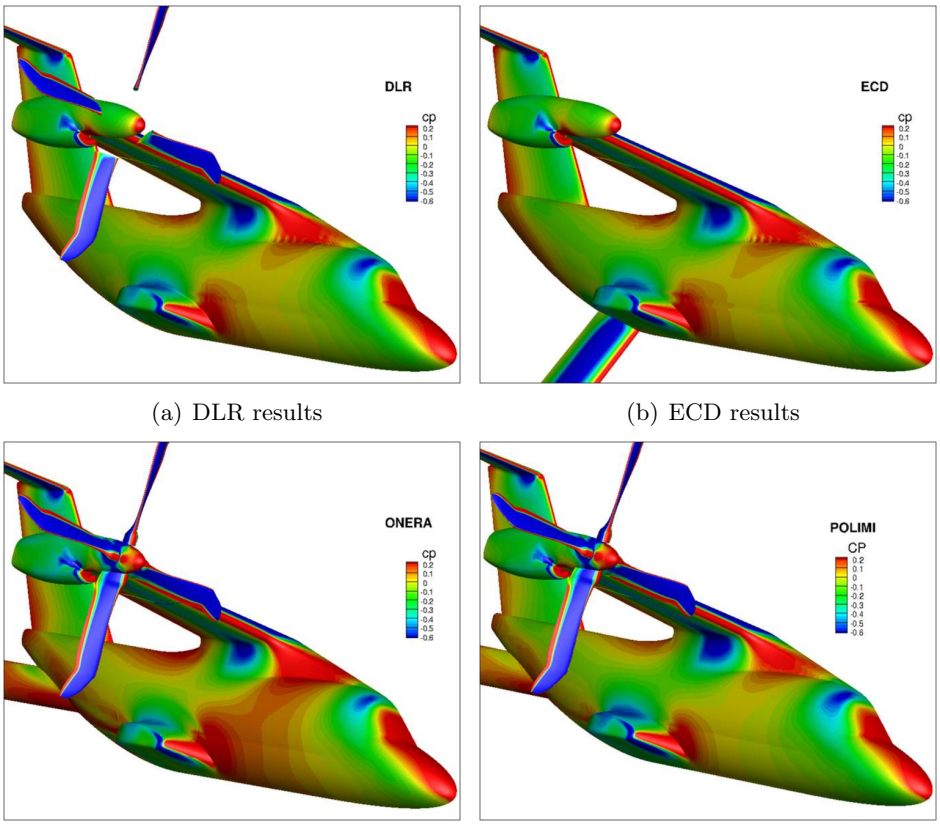

(a) DLR results (b) ECD results

(c) ONERA results (d) PoliMi results

Figure 10: Pressure field on the fuselage

Comparison between DLR and ECD results allow to state that the influence of the rotor model on the fuselage pressure is almost negligible, since the AD calculations gives the same pressure distribution as the fully unsteady calculations. They also produce similar results for the lift coefficient. Some quantitative differences are found instead in the drag coefficient values.

4.4 Rotor

The pressure distributions on the outer, lifting part of the blade (fig. 13) show a remarkable qualitative agreement among all computations, not being influenced by the blade root region. A slight lower level of suction on the blade upper side is observed in PoliMi results. The thrust variation with rotor azimuth, reported in fig. 14(a), is qualitatively very similar but with quantitative differences. Lower thrust predicted in PoliMi results may be partly explained by the highest value of V_∞ considered. Torque variation during one revolution is similar for ONERA and DLR results, while larger variations are shown by PoliMi results. This disagreement may involve the different turbulence model used ($k-\omega$ for ONERA/DLR, Spalart-Allmaras for PoliMi).

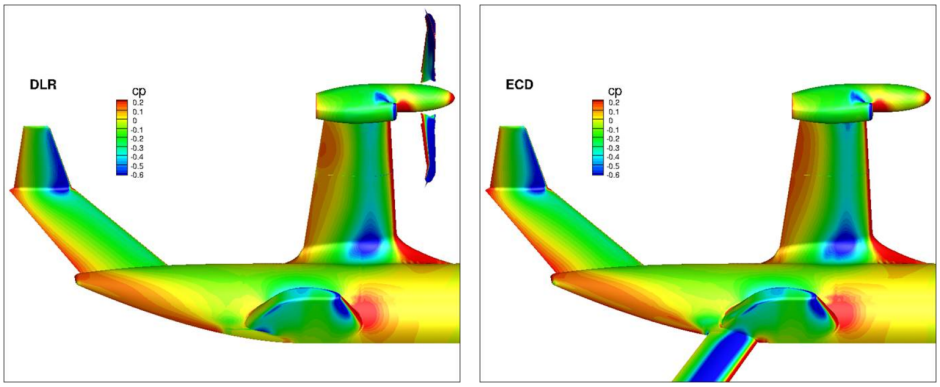

(a) DLR results (b) ECD results

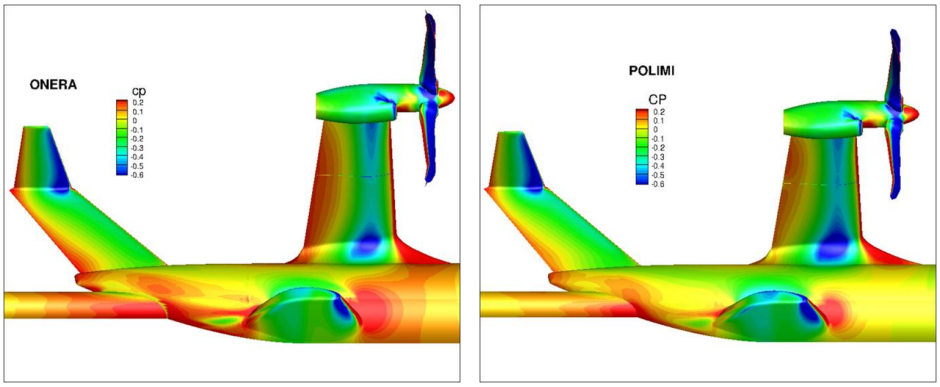

(c) ONERA results (d) PoliMi results

Figure 11: Pressure field on aft part of the fuselage

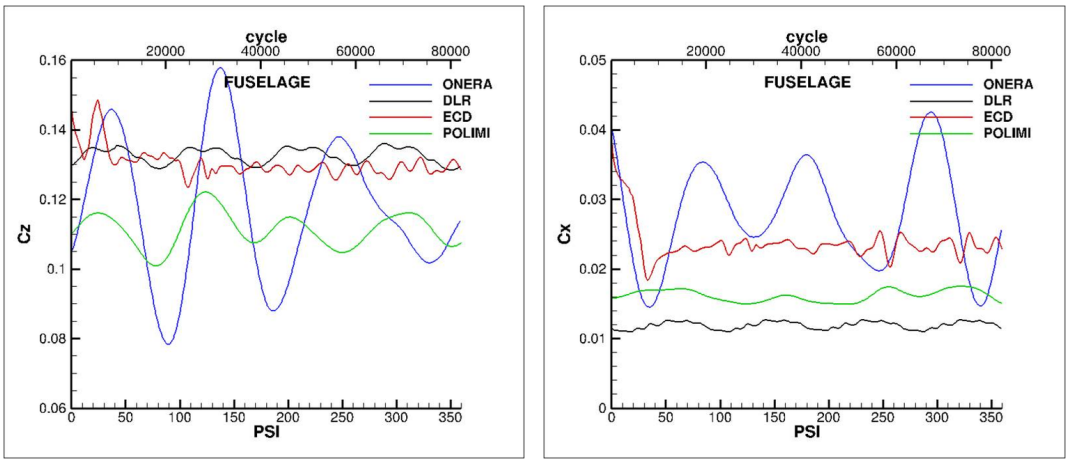

(a) Cz (b) Cx

Figure 12: Global loads on the fuselage

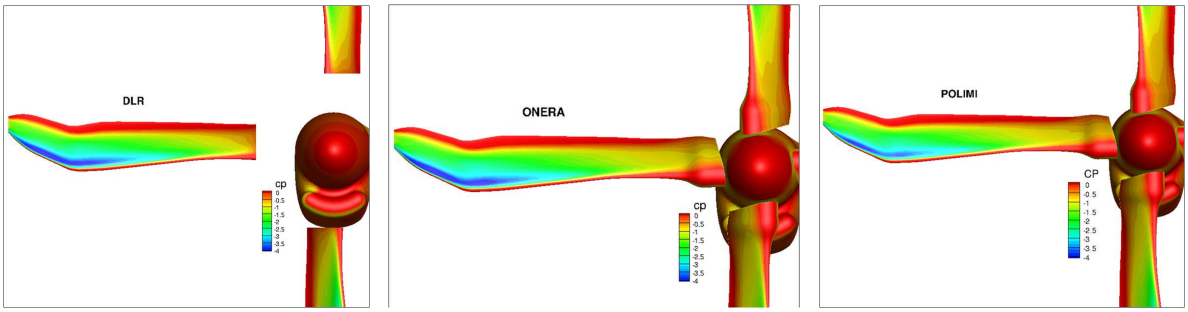

(a) DLR results (b) ONERA results (c) PoliMi results

Figure 13: Pressure field on the rotor blade

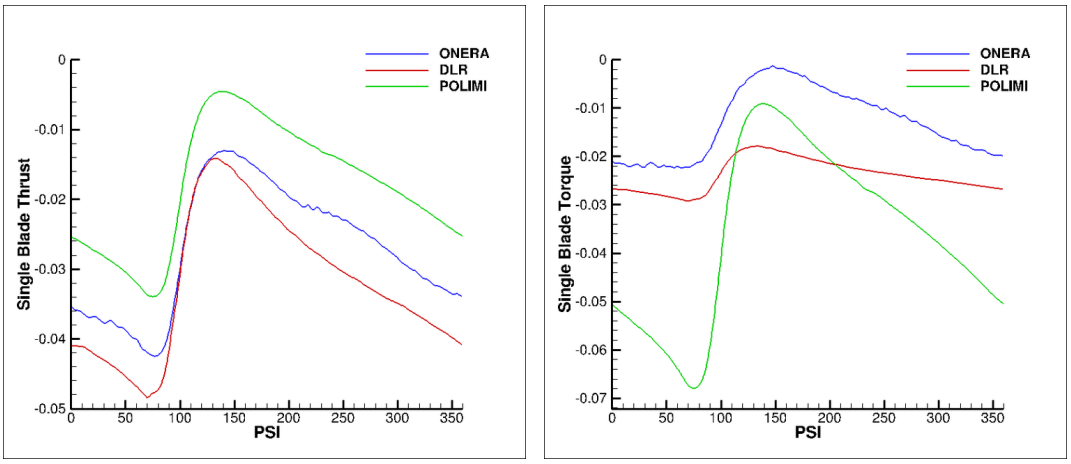

(a) Thrust coeff. (b) Torque coeff.

Figure 14: Global loads on the rotor blade

The large variation of thrust generated by a single blade during one rotor revolution is motivated by the strong induced velocity field of the tiltable wing. Remind that the $\psi = 0\,\text{deg}$ value corresponds to the lower vertical position of the reference blade, so that in the $\psi = 90\,\text{deg}$ position the blade is located close to the wing, which explain the large unsteady thrust and torque in this azimuth range.

The visualization of the rotor wake with the Q-criterion (fig. 15), taken from ONERA and PoliMi results gathered on the same grids, clearly shows the wake-wing interaction that takes place for the present aircraft mode configuration.

5 Conclusions

This work presented a global comparison of several blind-test numerical predictions of the aerodynamic field around the Erica model in aircraft mode, carried out by some Partners of the *NICETRIP* consortium, i.e. ONERA, DLR, ECD and PoliMi. The calculations are carried out with different codes, different turbulence models, different wind tunnel setups and different grids, with the objective of supporting the future experimental test campaign in the DNW-LLF and ONERA S1Ma wind tunnels. Furthermore, the comparison allow to assess the amount of scatter among the different code predictions.

Notwithstanding that a more thorough analysis should be completed, the comparison exercise allow to make the following conclusions: time-accurate calculations are required, inasmuch the level of unsteadiness introduced by the rotor wake on the aerodynamic loads on the fuselage, wing and nacelle may be relevant – with the only exception of the lift of the fuselage, where DLR and

ECD calculations, carried out with the same grid but different rotor models, give similar averaged results. It is also required to have a detailed description of the blade root, which dramatically influences the loads on the nacelle. The influence of the lower-mounted wind tunnel support is rather limited, while the rear-mounted support introduces some local unsteady effects on the fuselage loads. The overall qualitative agreement of the pressure distributions among different calculations is somewhat acceptable, while the scatter of the quantitative average loads is still important.

The comparison with the experimental results of the future wind tunnel campaign planned in 2013 should allow better understanding of the computational results. It is finally planned to study other flight conditions such as conditions in the conversion corridor where large aerodynamic interactions can appear.

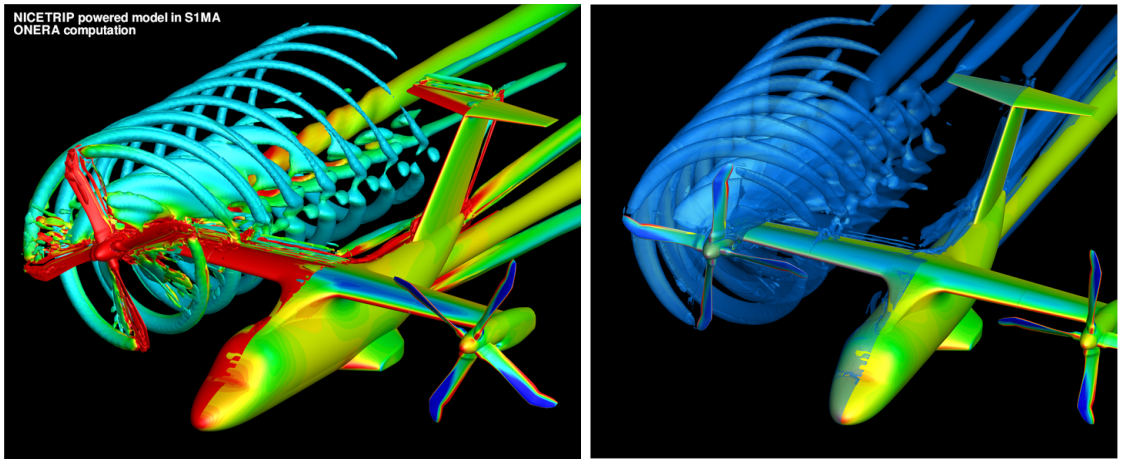

(a) ONERA (b) PoliMi

Figure 15: Rotor wake visualization with Q-criterion, ONERA/PoliMi grids

Aknowledgements: this work has been partially funded under the EC supported FP6/Aeronautics Project AIP5-CT-2006-03-944 *NICETRIP*.

References

[1] L. Cambier, S. Heib, and S. Plot. The ONERA elsA CFD software: input from research and feedback from industry. In 28^{th} *Congress of the International Council on the Aeronautical Sciences, Brisbane*, 2012.

[2] N. Kroll, B. Eisfeld, and H.M. Bleecke. The Navier-Stokes Code FLOWer. In *Notes on Numerical Fluid Mechanics, Vieweg, Braunschweig*, volume 71, pages 58–71, 1999.

[3] M. Biava. *RANS computations of rotor/fuselage unsteady interactional aerodynamics*. PhD thesis, Dipartimento di Ingegneria Aerospaziale, Politecnico di Milano, 2007.

[4] A. Jameson. Time dependent calculations using multigrid with applications to unsteady flows past airfoils and wings. In 10^{th} *AIAA Computational Fluid Dynamics Conference, Honolulu, HI. AIAA 91-1596*, 1991.

[5] P.L. Roe. Approximate Riemann solvers, parameter vectors and difference schemes. *J.Comput. Phys*, 43:357–372.

[6] V. Venkatakrishnan. On the accuracy of limiters and convergence to steady state solutions. In 31^{st} *AIAA Aerospace Sciences Meeting and Exhibit, Reno, NV. AIAA 93-0880*, 1993.

[7] D.C. Wilcox. Reassessment of the scale-determining equation for advanced turbulence models. *AIAA J.*, 26:1299–1310, 1988.

[8] J.C. Kok. Resolving the dependence on freestream values for the $k - \omega$ turbulence model. *AIAA J.*, 38:1292–1295, 2000.

[9] P.R. Spalart and S.R. Allmaras. One equation model for aerodynamic flows. In 30^{th} *AIAA Aerospace Science Meeting & Exhibit, Reno, NV. AIAA 92-0439*, 1992.

[10] J.A. Benek, J.L. Steger, and F.C. Dougherty. A flexible grid embedding technique with application to the Euler equations. In 6^{th} *Computational Fluid Dynamics Conference, Danvers, MA. AIAA 83-1944*, 1983.

[11] T. Schwarz. Development of a wall treatment for Navier-Stokes computations using overset-grid technique. In 26^{th} *European Rotorcraft Forum, The Hague, The Netherlands.*, 2000.

[12] G. Chesshire and W. D. Henshaw. Composite overlapping meshes for the solution of partial differential equations. *J. Comp. Phys.*, 90:1–64, 1990.

[13] W. M. Chan and P. G. Buning. Zipper grids for force and moment computation on overset grids. *AIAA Paper*, (95-1681-CP), 1995.